Materials Today Communications 38 (2024) 107845

Contents lists available at ScienceDirect

Materials Today Communications

journal homepage: www.elsevier.com/locate/mtcomm

Structural, mechanical, electronic and thermodynamic analysis of calcium aluminum silicate crystalline phases in stone wool insulation materials: A first-principles study

Thi H. Ho [a,b], Do Tuong Ha [c], Nguyen-Hieu Hoang [d], Øivind Wilhelmsen [e,f], Thuat T. Trinh [e,*]

[a] Laboratory for Computational Physics, Institute for Computational Science and Artificial Intelligence, Van Lang University, Ho Chi Minh City, Viet Nam
[b] Faculty of Mechanical - Electrical and Computer Engineering, School of Technology, Van Lang University, Ho Chi Minh City, Viet Nam
[c] Faculty of Applied Sciences, Ton Duc Thang University, Ho Chi Minh City, Viet Nam
[d] Department of Materials and Nanotechnology, SINTEF Industry, Norway
[e] Porelab, Department of Chemistry, Norwegian University of Science and Technology - NTNU, Norway
[f] Department of Gas Technology, SINTEF Energy Research, NO-7465, Trondheim, Norway

ARTICLE INFO

Keywords:
Calcium aluminum silicate
Elastic
Thermodynamics
DFT
Stone wool

ABSTRACT

Stone wool materials have gained considerable attention due to their effectiveness as thermal and acoustic insulation solutions. The comprehension of crystal structure properties is pivotal in determining the overall performance of these materials, as it enables us to optimize their composition for enhanced insulating capabilities. Crucial factors such as structural, mechanical, and thermodynamic characteristics of crystalline phases within stone wool are vital for evaluating its thermal and acoustic insulation properties. This study investigates the properties of calcium aluminum silicate crystal phases commonly present in stone wool, including anorthite, svyatoslavite, scolecite, and dehydrated scolecite using density functional theory (DFT) calculations. In comparison to previous works, this study provides a more comprehensive analysis using advanced DFT calculations. Our analysis reveals the complex interplay between the crystal structures and mechanical behavior of these phases. The calculated bulk modulus of the phases varies significantly, ranging from 38 to 83 GPa. We have compared the calculated elastic properties with available experimental data and found excellent agreement, confirming the accuracy of the computational approach. Moreover, we find that polymorphism has a significant impact on the mechanical strength, with anorthite exhibiting higher strength compared to svyatoslavite. Furthermore, dehydration is found to cause a reduction in unit volume and mechanical strength. The thermodynamic properties of dehydrated scolecite, including entropy and heat capacity, are significantly lower due to the absence of water molecules. These findings highlight the importance of understanding the structural and mechanical characteristics of calcium aluminum silicate phases in stone wool materials. Additionally, our findings have broader implications in various industries requiring effective insulation solutions such as to develop new materials or to enhance the energy efficiency of existing insulating products.

1. Introduction

Stone wool is an insulation material widely used in various industries due to its excellent thermal and acoustic properties [1,2]. It is derived from volcanic rock or industrial waste materials, which are melted and then spun into fibers. These fibers are next bound together to form a versatile and durable insulation product [3]. Stone wool is a highly effective insulation material known for its exceptional thermal resistance properties. It exhibits a low thermal conductivity, meaning that it significantly reduces heat transfer by conduction. The unique structure of stone wool, composed of fine and mostly continuous fibers, traps air within its matrix. The trapped air creates an insulating barrier that resists the transfer of heat. As a result, stone wool insulation helps to maintain stable indoor temperatures by preventing heat loss during colder months and heat gain during hotter periods. This property makes stone wool insulation an excellent choice for enhancing the energy efficiency of buildings and industrial equipment [1,2].

Substantial progress has been made in characterizing and inferring stone wool fiber structure at micrometer resolution [4,5]. The structure of stone wool has been recently investigated by Ivanič et al. [6] using different techniques such as scanning electron microscopy (SEM), transmission electron microscopy (TEM). They investigated the surface

* Corresponding author.
E-mail addresses: thi.hohuynh@vlu.edu.vn (T.H. Ho), thuat.trinh@ntnu.no (T.T. Trinh).

https://doi.org/10.1016/j.mtcomm.2023.107845
Received 29 August 2023; Received in revised form 5 December 2023; Accepted 9 December 2023
Available online 12 December 2023

morphology of stone wool fibers at the micrometer scale and the nanometer scale. In particular, knowledge of the atomic-scale structure of stone wool fiber surfaces is essential for understanding and manipulating the properties of this material in a range of applications, such as how stone wool fibers behave in insulation at ambient humidity [7]. This information allows us to optimize the design for enhanced insulating capabilities and improve the overall performance of the fiber materials in various applications [8–10].

The structure of stone wool consists of an interconnected and porous fiber network characterized by a high porosity of approximately 98% [4,5]. These fibers have a composition similar to that of rock, specifically calcium aluminosilicate (CAS) with the chemical component composed of (CaO-Al_2O_3-SiO_2). The study of CAS materials is closely linked to the research on stone wool due to the fundamental role CAS plays in its composition and properties. The CAS serves as building blocks for the interwoven fibers of stone wool, providing it with desirable thermal resistance and insulation properties. In the realm of stone wool fiber research, CAS has often been utilized as a model system [7]. The structure of CAS, specifically in the context of stone wool, has been investigated by examining minerals such as anorthite and scolecite as representative of perfect crystal models for stone wool.

Anorthite ($CaAl_2Si_2O_8$), a calcium aluminum silicate mineral [11,12], is characterized by its closely related composition to CAS and serves as a valuable model for understanding the structural features of stone wool. Svyatoslavite ($CaAl_2Si_2O_8$) is a fascinating polymorph of the mineral anorthite, belonging to the plagioclase feldspar group [13]. Polymorphism refers to the phenomenon where a chemical compound can exist in multiple crystal structures while maintaining the same chemical composition. In the case of anorthite, svyatoslavite emerges as an alternative crystal structure to the more commonly known forms. Characterizing the crystal structure and properties of svyatoslavite is essential for comprehending its unique behavior and potential applications. Scolecite ($CaAl_2Si_3O_{10}.3H_2O$), a hydrated calcium aluminum silicate mineral that belongs to the zeolite material group [14], has been selected as another model for stone wool due to its similar composition and crystal structure. The impact of water molecules and their interaction with the CAS network in stone wool insulation can be obtained by examining scolecite as a representative crystal model. Thus, the utilization of anorthite and scolecite as perfect (without defects in the structure) crystal models for stone wool offers a deeper understanding of the structural characteristics, bonding arrangements, and potential hydration effects within the CAS framework. This knowledge contributes to unravel the underlying factors governing the thermal, mechanical, and moisture-related properties of stone wool, ultimately aiding in the optimization and development of more efficient and tailored insulation materials.

Molecular dynamics simulations have been extensively employed to investigate the structure, dynamics, and behavior of CAS materials, yielding valuable insights into their properties [15–18]. However, the application of Density Functional Theory (DFT) simulations in the context of atomic-scale structural characterization of CAS phases, particularly in stone wool fibers, has been relatively limited. Both the bulk structure and surface structure of CAS materials in stone wool fibers remain poorly understood in terms of their atomic-scale features. The work of Tian et al. [19] presented a model of anorthite glass. Both crystalline and amorphous structures of anorthite were examined using ab initio molecular dynamics simulations, and the results were found to be consistent with experimental observations. However, the periodic modeling approach employed in the work of Tian et al. [19] failed to generate acceptable fracture surfaces. To overcome this limitation, isolated molecular cluster models of anorthite were proposed [19]. A recent study by Zhang et al. [20] delves into the field of periodic DFT, specifically focusing on the adsorption behavior of CO_2 on the anorthite (001) surface and the influence of water molecules in the process. By conducting comprehensive DFT simulations, the authors [20] aim to elucidate the interactions between CO_2 and the anorthite surface while investigating the impact of water on the adsorption process. Ghosh et al. performed ab initio molecular dynamics simulations to calculate the bulk modulus of CAS material, as described in their study [21]. However, a significant discrepancy was observed between the calculated bulk modulus and the experimental values [22,23].

Understanding the interaction between water molecules and the zeolite framework, such as scolecite, is crucial for comprehending the structure and mechanical properties of the material. The presence of water within the scolecite structure makes it necessary to investigate its behavior and effects. Fischer et al. [24] conducted a significant study on this matter, specifically focusing on the utilization of dispersion-corrected approaches in DFT calculations. Their research demonstrated the importance of employing these approaches to accurately describe the behavior of water molecules within the scolecite framework. Furthermore, the role of water in influencing the elastic properties of various zeolite structures, including scolecite, was investigated by Bryukhanov et al. [25]. Their work highlights the significance of considering both the presence and absence of water in studying the structure and elastic properties of zeolite. However, it is important to note that their simulations were unable to obtain the structure of dehydrated scolecite, which limits the understanding of the complete behavior of scolecite in the absence of water.

This study aims to address limitations present in prior research, specifically focusing on the lack of a comprehensive understanding of CAS crystal phases within stone wool materials and the absence of investigation into the role of water molecules in scolecite structures. By employing DFT simulations, this work investigates four distinct CAS models of stone wool fiber: anorthite, svyatoslavite, scolecite, and the dehydrated scolecite. The primary objective is to elucidate the elastic and thermodynamic properties exhibited by these phases, with particular emphasis on the influence of water on their properties. The investigation explores the elastic properties of these phases, encompassing parameters such as the bulk modulus, Young's modulus, and shear modulus. Additionally, the thermodynamic properties, including entropy, enthalpy, and specific heat capacity, are evaluated. Notably, the focus of this study lies in elucidating the role of water in influencing the properties of CAS structures. Water molecules are inherently present in the scolecite and dehydrated scolecite models, allowing for an in-depth investigation of their interaction with the CAS framework. The paper is organized as follows: Computational methods and models are presented in Section 2. Section 3 discusses the obtained results. Finally, concluding remarks are summarized in Section 4.

2. Models and methods

The selection of an appropriate initial structure is crucial for accurate simulations and reliable results. In this study, the experimental data available for anorthite, svyatoslavite and scolecite served as the basis for constructing the initial atomic configurations. The initial crystal structures were obtained from the American Mineralogist Crystal Structure Database [26]. The crystal structure system of anorthite is triclinic, whereas that of svyatoslavite and scolecite is monoclinic. By aligning with experimental observations, this approach ensures that the simulated CAS structures closely resemble their real-world counterparts. However, the unique crystal structure of scolecite poses computational challenges due to its extensive unit cell. Recognizing the importance of computational efficiency without compromising the quality of the simulations, we strategically adopted the use of a primitive cell. The primitive cell represents the fundamental repeating unit of the crystal lattice, containing the essential information required to describe the entire crystal structure. By employing the primitive cell, we significantly reduce the computational complexity associated with the simulation of scolecite. Moreover, employing a primitive cell retains the essential features and characteristics of the scolecite structure,

ensuring that the simulated results remain representative and accurate in the Density Functional Theory (DFT) simulations.

DFT calculations were performed using the Vienna Ab initio Simulation Package (VASP) software [27,28]. The Perdew–Burke–Ernzerhof (PBE) exchange–correlation functional was employed to describe the electronic structure and energetics of the systems under investigation. The PBE functional is one of the most common DFT methods in solid state calculation and was previously applied to study the properties of solid cement clinker phases [29,30]. It has been demonstrated that the inclusion of Van der Waals (VdW) corrections in DFT calculations plays a significant role in obtaining accurate results for silicate material [29–31]. The DFT-D2 method of Grimme et al. [32] was employed to add VdW correction in this study. This methodology has proven effective in capturing long-range dispersion to gain a comprehensive understanding of structural and mechanical characteristics of material [31,32]. We denote our method as DFT-PBE-D2. The previous work of Mai et al. [31] has shown that this DFT-PBE-D2 performs better than the Local Density Approximation (DFT-LDA). In the remaining part of this paper, the term DFT refers to the specific method DFT-PBE-D2 unless otherwise specified.

The atomic positions and crystal parameters (3 lattice parameters a, b, c and 3 angles α, β, γ) were relaxed using the DFT optimization algorithm implemented in VASP. The convergence criterion for energy was set to 1.0×10^{-6} eV to ensure accurate calculations. The Monkhorst–Pack k-point mesh was used for Brillouin zone sampling, with a density appropriate for the specific system. A plane-wave basis set was used with an energy cutoff of 600 eV. This energy cutoff was chosen based on convergence tests to balance accuracy and computational efficiency. The structures of the phases were plotted using the VESTA package [33]. The electronic properties of the materials were investigated with the calculation of density of state (DOS).

In order to evaluate the elastic properties of the CAS phases, we used an established method outlined briefly here. The generalized Hooke's Law for a linear elastic material is written as:

$$\begin{bmatrix} \sigma_1 = \sigma_{xx} \\ \sigma_2 = \sigma_{yy} \\ \sigma_3 = \sigma_{zz} \\ \sigma_4 = \sigma_{yz} \\ \sigma_5 = \sigma_{xz} \\ \sigma_6 = \sigma_{xy} \end{bmatrix} = \begin{bmatrix} C_{11} & C_{12} & C_{13} & C_{14} & C_{15} & C_{16} \\ C_{21} & C_{22} & C_{23} & C_{24} & C_{25} & C_{26} \\ C_{31} & C_{32} & C_{33} & C_{34} & C_{35} & C_{36} \\ C_{41} & C_{42} & C_{43} & C_{44} & C_{45} & C_{46} \\ C_{51} & C_{52} & C_{53} & C_{54} & C_{55} & C_{56} \\ C_{61} & C_{62} & C_{63} & C_{64} & C_{65} & C_{66} \end{bmatrix} \begin{bmatrix} \varepsilon_1 = \varepsilon_{xx} \\ \varepsilon_2 = \varepsilon_{yy} \\ \varepsilon_3 = \varepsilon_{zz} \\ \varepsilon_4 = \varepsilon_{yz} \\ \varepsilon_5 = \varepsilon_{xz} \\ \varepsilon_6 = \varepsilon_{xy} \end{bmatrix} \tag{1}$$

This notation with only one subscript for the stress and strain, numbered from 1…6, is helpful as it allows the equations of anisotropic elasticity to be written in matrix form. The 36's C_{ij} are called the stiffnesses. The matrix of stiffnesses is called the stiffness matrix. This matrix can be inverted so that the strains are given explicitly in terms of the stresses:

$$\begin{bmatrix} \varepsilon_1 \\ \varepsilon_2 \\ \varepsilon_3 \\ \varepsilon_4 \\ \varepsilon_5 \\ \varepsilon_6 \end{bmatrix} = \begin{bmatrix} S_{11} & S_{12} & S_{13} & S_{14} & S_{15} & S_{16} \\ & S_{22} & S_{23} & S_{24} & S_{25} & S_{26} \\ & & S_{33} & S_{34} & S_{35} & S_{36} \\ & & & S_{44} & S_{45} & S_{46} \\ & & & & S_{55} & S_{56} \\ & & & & & S_{66} \end{bmatrix} \begin{bmatrix} \sigma_1 \\ \sigma_2 \\ \sigma_3 \\ \sigma_4 \\ \sigma_5 \\ \sigma_6 \end{bmatrix} \tag{2}$$

The stiffness constants C_{ij} and constituents of the compliance tensor S_{ij} were calculated using VASP. From the calculated C_{ij} and S_{ij}, the polycrystalline corresponding bulk modulus K and shear modulus G are determined using the Voigt–Reuss–Hill (VRH) approximation, as shown in Eqs. (3) and (4). In these equations, the underscripts R and V denote Reuss and Voigt bounds, respectively.

$$\begin{aligned} K_R &= \frac{1}{S_{11} + S_{22} + S_{33} + 2(S_{12} + S_{23} + S_{31})} \\ K_V &= \frac{C_{11} + C_{22} + C_{33} + 2(C_{12} + C_{23} + C_{31})}{9} \\ K &= \frac{K_R + K_V}{2} \end{aligned} \tag{3}$$

$$\begin{aligned} G_R &= \frac{15}{4(S_{11} + S_{22} + S_{33}) - 4(S_{12} + S_{23} + S_{31}) + 3(S_{44} + S_{55} + S_{66})} \\ G_V &= \frac{C_{11} + C_{22} + C_{33} - (C_{12} + C_{23} + C_{31}) + 3(C_{44} + C_{55} + C_{66})}{15} \\ G &= \frac{G_R + G_V}{2} \end{aligned} \tag{4}$$

The Young's modulus, E, and Poisson's ratio, ν, for an isotropic material can then be estimated by:

$$E = \frac{9KG}{3K + G}, \quad \nu = \frac{3K - 2G}{6K + 2G} \tag{5}$$

The directional elastic constants were also obtained in this work. The computational approach is based on the theoretical framework and implementation described in the original work [34]. The spacial dependence of mechanical properties was plotted using the Elate package [34]. The Bulk/Shear ratio, also known as Pugh's ratio or Pugh's criterion, is a dimensionless parameter used to assess the mechanical stability and ductility of crystalline materials. It provides a measure of the resistance to volume change (bulk modulus) relative to the resistance to shape change (shear modulus) under applied stress. The ratio provides insight into the ability of a material to withstand deformation under different stress conditions. A lower value of Pugh's ratio indicates a higher resistance to volumetric deformation compared to shear deformation, implying a more brittle behavior. Conversely, a higher value of Pugh's ratio suggests a greater ability to undergo plastic deformation, indicating a more ductile or malleable material [35].

The Universal Elastic Anisotropy Index (A^U) is a metric used to quantify the degree of anisotropy, or directional dependence, in the elastic properties of materials [36]. Elastic anisotropy refers to the variation in mechanical behavior along different crystallographic directions in a crystalline material. The A^U is based on the idea that the elastic properties of a material can be described by a tensor, which is a mathematical object that captures the directional dependence of these properties. The index provides a single value that represents the overall anisotropy of a material's elastic properties. The index is typically calculated using elastic constants or stiffness coefficients obtained from experimental measurements or theoretical calculations. These constants describe how a material deforms under applied stress or strain in different directions. By comparing the magnitudes of the elastic constants along different crystallographic axes, the A^U can be determined. A value of 0 for the A^U index indicates isotropic behavior, meaning that the material has the same mechanical properties in all directions. On the other hand, a higher value indicates anisotropy, suggesting that the material's mechanical properties vary significantly depending on the direction [37].

Thermodynamic calculations were performed using the Phonons from Finite Differences method implemented in the VASP software [27,28]. This approach allows for the determination of phonon frequencies and related properties, which are essential for studying the thermodynamic behavior of materials. To begin the calculations, the equilibrium lattice parameters and atomic positions obtained from the DFT optimization were used as the starting point. The force constants between atoms were calculated using finite differences, which involves displacing the atoms from their equilibrium positions and calculating the resulting forces on each atom. These displacements and forces were used to construct the dynamical matrix, which describes the interatomic force constants and determines the phonon frequencies.

Based on the phonon frequencies, various thermodynamic properties were calculated, including the phonon density of states, Helmholtz free energy, specific heat capacity, and entropy. These properties provide insights into the vibrational and thermal behavior of the system. The calculations were typically performed at different temperatures to examine the temperature dependence of the thermodynamic quantities.

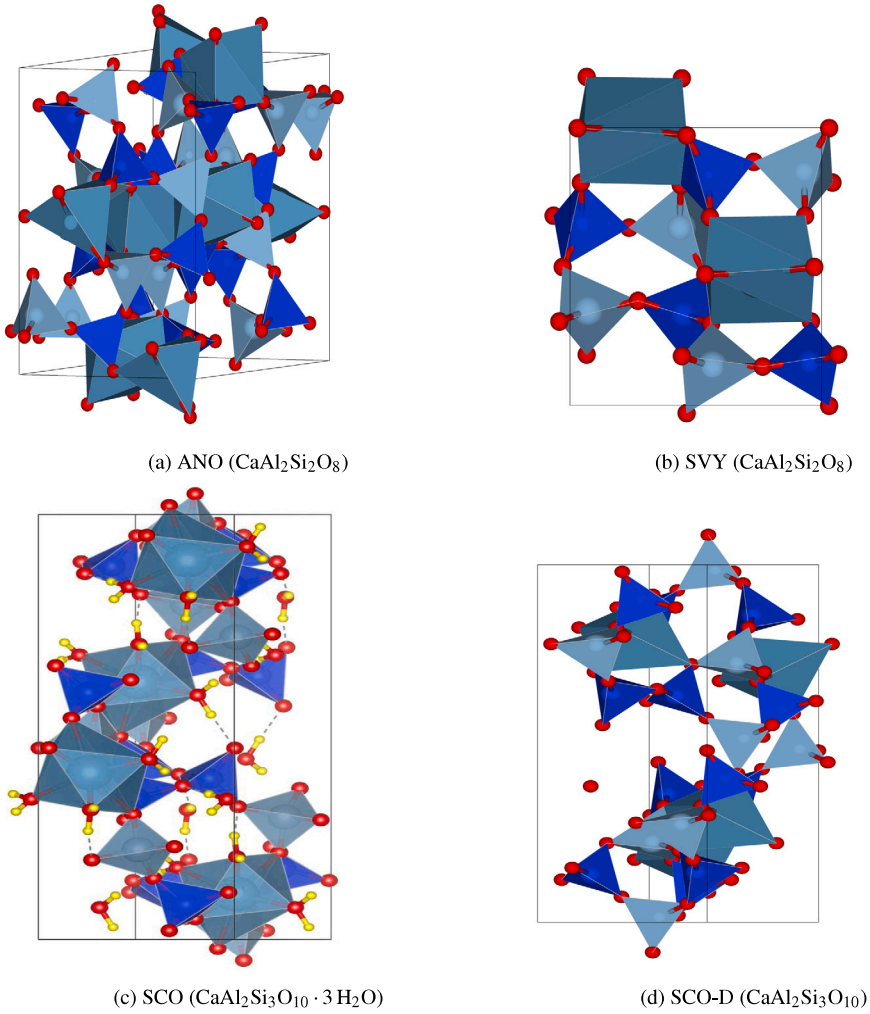

Fig. 1. Optimized conventinal cell of crystal structure obtained from DFT-PBE-D2 calculations: anorthite ANO (a), svyatoslavite SVY (b), scolecite SCO (c), and Dehyrated scolecite SCO-D (d).

It is important to note that these calculations assume a harmonic approximation, neglecting anharmonic effects such as phonon–phonon interactions. However, the harmonic approximation is generally sufficient for studying the thermodynamics of solids under normal conditions.

In addition to analyzing structural, mechanical, and thermodynamic properties, we have also computed electronic properties using DFT calculations. Specifically, we determined the density of states and band gaps for each CAS phase under investigation.

For brevity and convenience, we will adopt the following abbreviations for the crystal names throughout the remainder of this study: anorthite (ANO), svyatoslavite (SVY), scolecite (SCO), and Dehydrated scolecite (SCO-D). The initial crystal structures for the three phases (ANO, SVY, SCO) were obtained from experimental data. These experimental structures serve as the starting point for subsequent calculations and analysis. The crystal of dehydrated phase SCO-D has not been found in the literature.

The crystal structures of ANO and SVY were already in the primitive cell form, which is advantageous for DFT calculations. However, the structures of SCO and SCO-D were initially in a non-primitive cell configuration. To ensure consistency and facilitate calculations, we transformed the structures of SCO and SCO-D to their respective primitive cells before proceeding with further analysis (See Fig. 1).

Table 1
Comparison between theoretical calculated crystal parameters and experimental values for the ANO and SVY phase. Experimental data [11–13] are provided for comparison, with values in parentheses indicating the relative deviation from the experimental data.

Parameter	ANO Exp. [11,12]	ANO DFT (this work)	SVY Exp. [13]	SVY DFT (this work)
a (Å)	8.173	8.200 (0.3%)	8.220	8.260 (0.5%)
b (Å)	12.869	12.936 (0.5%)	8.951	8.650 (−3.4%)
c (Å)	14.165	14.214 (0.3%)	4.828	4.838 (0.2%)
α (°)	93.113	93.111 (−0.0%)	90.000	90.000 (0.0%)
β (°)	115.913	115.727 (−0.2%)	90.000	89.971 (−0.0%)
γ (°)	91.261	91.421 (0.2%)	90.000	90.000 (0.0%)
Volume (Å^3)	1336.3	1354.4 (1.3%)	355.2	345.7 (−2.7%)

3. Results and discussions

3.1. Structural properties

The structural properties of ANO and SVY, including lattice parameters and unit cell volumes, were thoroughly investigated and are summarized in Table 1. The optimization process using DFT calculations yielded highly accurate results, exhibiting excellent agreement with experimental data. For ANO, the calculated crystal parameters

Table 2
Comparison between theoretical calculated crystal parameters and experimental values for the SCO and SCO-D. The values in parentheses indicate the relative deviation from the experimental data of SCO [14]. Note that experimental unit cell was converted into primitive cell (see method section).

Parameter	SCO (Exp.)	SCO (DFT, this work)	SCO-D (DFT, this work)
a (Å)	10.060	10.062 (0.0%)	9.390 (−6.7%)
b (Å)	10.060	10.062 (0.0%)	9.390 (−6.7%)
c (Å)	9.772	9.836 (0.7%)	8.813 (−9.8%)
α (°)	96.064	83.805 (−12.8%)	94.768 (−1.3%)
β (°)	96.064	83.805 (−12.8%)	94.768 (−1.3%)
γ (°)	142.105	142.124 (0.0%)	139.497 (−1.8%)
Volume (Å^3)	574.4	576.7 (0.4%)	490.0 (−14.7%)

deviated by less than 1% from the expected values, demonstrating the remarkable precision of the DFT method in predicting its structural properties. Similarly, for SVY, the computed values display a deviation of less than 5% compared to experimental data, further affirming the reliability of the DFT approach. These findings demonstrate the effectiveness and robustness of DFT in characterizing the structural properties of ANO and SVY phases.

Table 2 provides a comprehensive comparison between the optimized unit cell parameters of the primitive cell for SCO and SCO-D and the corresponding experimental data. It is worth noting that the structure of SCO-D has not been observed experimentally, nor has it been characterized through previous calculations. For the SCO structure, the DFT optimization yielded remarkable agreement with experimental measurements, particularly in terms of the cell lengths, with a deviation of less than 1%. However, slight differences of up to 13% were observed in the angles between the crystal axes. Nevertheless, it is crucial to highlight that the volumetric changes between the calculated and experimental values were minimal, amounting to only 0.4%. This exceptional agreement in terms of volume indicates a high accuracy and reliability of the DFT method in capturing the overall structural characteristics of SCO.

Moreover, while the experimental characterization of SCO-D is lacking, the comparison with the SCO structure suggests the need of further investigations to elucidate the structural properties of this intriguing phase. The dehydrated structure SCO-D was optimized using the DFT method, revealing a significant reduction in cell parameters and volume compared to the hydrated form, SCO. The values presented in Table 2 illustrate these changes in detail. Specifically, the length of the unit cell experiences a reduction of approximately 10%, while the angles of the unit cell remain unchanged. Furthermore, the volume of the unit cell decreases by 15%. These findings highlight the substantial impact of water absence on the crystalline structure, as evidenced by the considerable volume reduction in SCO upon dehydration. The observed reduction in cell parameters and volume can be attributed to the removal of water molecules from the crystalline framework. Water molecules occupy space within the structure, and their removal leads to a more compact arrangement of atoms, resulting in reduced cell dimensions and volume. The preservation of the unit cell angles suggests that the removal of water does not significantly alter the crystal lattice geometry, maintaining the crystal's internal symmetry.

The optimized DFT calculations demonstrate that the removal of water from the SCO structure results in a considerable reduction in cell parameters and volume. These findings shed light on the structural changes induced by dehydration and provide valuable insights into the role of water molecules in determining the volumetric properties of crystalline materials.

3.2. Mechanical properties

The determination of elastic properties provides valuable insights into the structural stability and mechanical behavior of materials. These properties are crucial for understanding the response of CAS phases to external forces, such as pressure or deformation. By comparing the calculated elastic properties with experimental data, we can assess the accuracy and reliability of the computational methods used in this study. This section focuses on the characterization of the mechanical properties of the CAS phases, particularly their elastic properties. The calculated elastic properties, including the bulk modulus, Young's modulus, and shear modulus, are presented and compared with the available experimental data. It is important to note that the literature predominantly reports the bulk modulus values for CAS phases, with limited information available on other elastic properties. Therefore, this study aims to bridge this knowledge gap by providing comprehensive calculations of these elastic properties for the CAS phases.

Table 3
Calculated elastic stiffness constants C_{ij} (GPa) of ANO. See Eq. (1) for more details on the direction of i,j notation.

C_{ij}	1	2	3	4	5	6
1	124.6	52.4	60.5	−10.4	3.4	1.4
2	52.4	181.1	38.3	−12.6	−0.9	14.0
3	60.5	38.3	160.8	−9.6	2.4	−11.0
4	−10.4	−12.6	−9.6	34.3	8.9	3.5
5	3.4	−0.9	2.4	8.9	29.1	0.9
6	1.4	14.0	−11.0	3.5	0.9	39.4

Table 4
Calculated elastic stiffness constants C_{ij} (GPa) of SVY. See Eq. (1) for more details on the direction of i,j notation.

C_{ij}	1	2	3	4	5	6
1	146.3	51.1	37.8	0.0	0.0	5.2
2	51.1	135.5	51.5	0.0	0.0	0.3
3	37.8	51.5	94.4	0.0	0.0	−0.1
4	0.0	0.0	0.0	47.9	4.4	0.0
5	0.0	0.0	0.0	4.4	49.7	0.0
6	5.2	0.3	−0.1	0.0	0.0	34.0

Table 5
Calculated elastic stiffness constants C_{ij} (GPa) of SCO. See Eq. (1) for more details on the direction of i,j notation.

C_{ij}	1	2	3	4	5	6
1	91.1	36.9	33.6	−0.1	1.0	−0.5
2	36.9	103.1	33.7	4.7	−0.2	0.8
3	33.6	33.7	81.6	0.0	9.3	3.2
4	−0.1	4.7	0.0	28.9	0.1	−1.1
5	1.0	−0.2	9.3	0.1	33.3	−5.3
6	−0.5	0.8	3.2	−1.1	−5.3	47.0

Table 6
Calculated elastic stiffness constants C_{ij} (GPa) of SCO-D. See Eq. (1) for more details on the direction of i,j notation.

C_{ij}	1	2	3	4	5	6
1	104.0	27.8	25.6	0.0	0.0	−15.2
2	27.8	70.9	18.3	0.0	0.0	−3.7
3	25.6	18.3	45.4	0.0	0.0	5.0
4	0.0	0.0	0.0	20.0	−5.5	0.0
5	0.0	0.0	0.0	−5.5	39.6	0.0
6	−15.2	−3.7	5.0	0.0	0.0	24.3

Table 3 provides a comprehensive summary of all the calculated elastic constants C_{ij} for the ANO structure. Our analysis reveals that the values of C_{11}, C_{22}, and C_{33} are in the range of 125-181 GPa, indicating that the material possesses similar levels of stiffness in these directions. This suggests that ANO exhibits isotropic behavior with respect to compression along these axes. However, the material is expected to be less compressive in the second direction, as evidenced by the high value of C_{22} compared to C_{11} and C_{33}. Furthermore, the ANO structure exhibits a high resistance to shear deformation along the third direction, as indicated by the highest shear modulus C_{66} when compared to C_{44} and C_{55}. This high shear resistance is attributed to the anisotropic

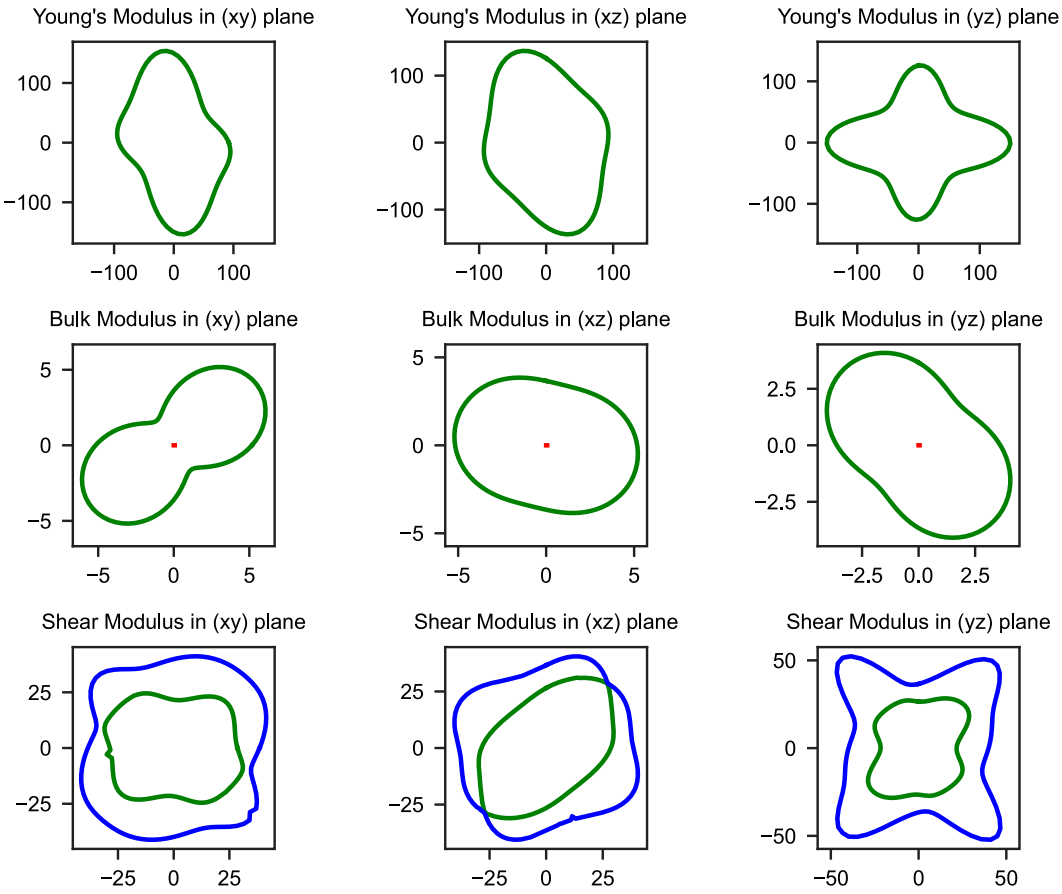

Fig. 2. Calculated spatial dependence of Young's modulus, Bulk modulus, and shear modulus (blue and green indicate the maximum and minimum values, respectively) of ANO. (For interpretation of the references to color in this figure legend, the reader is referred to the web version of this article.)

nature of the material, which is reflected in the directional elastic moduli plot shown in Fig. 2 . As seen in this figure, all moduli exhibit marked directional dependence, with significant variations observed between the different directions. This anisotropic behavior arises from the inherent structural asymmetry of the material, which affects its mechanical response under different loading conditions. In Table 3, we observed several small negative values in cross terms of the elastic stiffness coefficient C_{ij}. These discrepancies are primarily attributable to numerical errors or approximations inherent in DFT calculations when assessing crystal deformation during stress–strain analysis. In fact, similar findings have been reported in the field. For example, Zaoui [38] also observed several negative cross term values for calcium silicate hydrate materials using DFT calculations. Thus, these small discrepancies do not impact the overall accuracy or reliability of the results regarding the mechanical properties of CAS phases present in stone wool materials.

Table 4 presents the elastic constants C_{ij} for the SVY structure. The values of C_{11}, C_{22}, and C_{33} are in the range of 94.4-146.3 GPa, indicating a relatively stiff material in these directions. The highest stiffness is observed in the first direction (C_{11}), followed by the second direction (C_{22}), and then the third direction (C_{33}). This suggests that SVY exhibits an anisotropic response to compressive forces, with greater resistance in the first direction (Fig. 3). The shear moduli C_{44}, C_{55}, and C_{66} are relatively lower compared to the stiffness constants. This indicates that SYV may have a lower resistance to shear deformation, especially along the C_{66} directions. The values of zero for off-diagonal C_{ij} indicate that there is no coupling between the corresponding strains and stresses in these directions. This suggests that SYV is relatively isotropic in terms of these elastic properties (Fig. 3).

Table 5 presents the elastic constants C_{ij} for the SOC structure. Analyzing the values in the table, we observe that the elastic constants for SOC range from approximately 81.6 to 103.1 GPa for the diagonal elements C_{11}, C_{22}, and C_{33} represent the stiffness along the principal crystallographic axes. The values correspond to shear moduli (C_{44}, C_{55}, and C_{66}) are in lower range from 28.9 to 47.0 GPa. These values of the elastic constants of SCO are smaller than that of ANO and SVY phases.

The elastic constants of SOC-D are presented in Table 6. The elastic constants of SOC and SOC-D exhibit notable differences due to dehydration. In SOC, the material demonstrates an initial stiffness in the first direction (C_{11}) of 91.1 GPa, while becoming more stiff in the second direction (C_{22}) with a value of 103.1 GPa. Upon dehydration, SOC-D undergoes changes in the elastic constants, showing increased stiffness in the first direction (C_{11}) with a value of 104.0 GPa. However, the second direction (C_{22}) experiences a significant reduction in stiffness, dropping to 70.9 GPa. These variations highlight the role of dehydration in altering the mechanical properties of SOC, affecting its response to different types of loading and its overall structural integrity. The shear resistance of SOC and SOC-D, as reflected in their shear modulus values (C_{44} and C_{55}), provides insights into their ability to withstand shear stress and deformation. The dehydration of SOC to form SOC-D decreases significantly the shear moduli. This reduction can be attributed to the removal of water molecules, which may contribute to the intermolecular interactions and structural stability of SOC. The decrease in shear resistance suggests that the dehydration process weakens the material's ability to resist shear deformations and may render it more susceptible to shear-induced failures. Therefore, understanding the changes in shear resistance due to dehydration is crucial for predicting the mechanical behavior and stability of SOC and its potential applications in various engineering and material science fields.

Comparing the calculated elastic properties with experimental results is essential for validating the accuracy of the computational

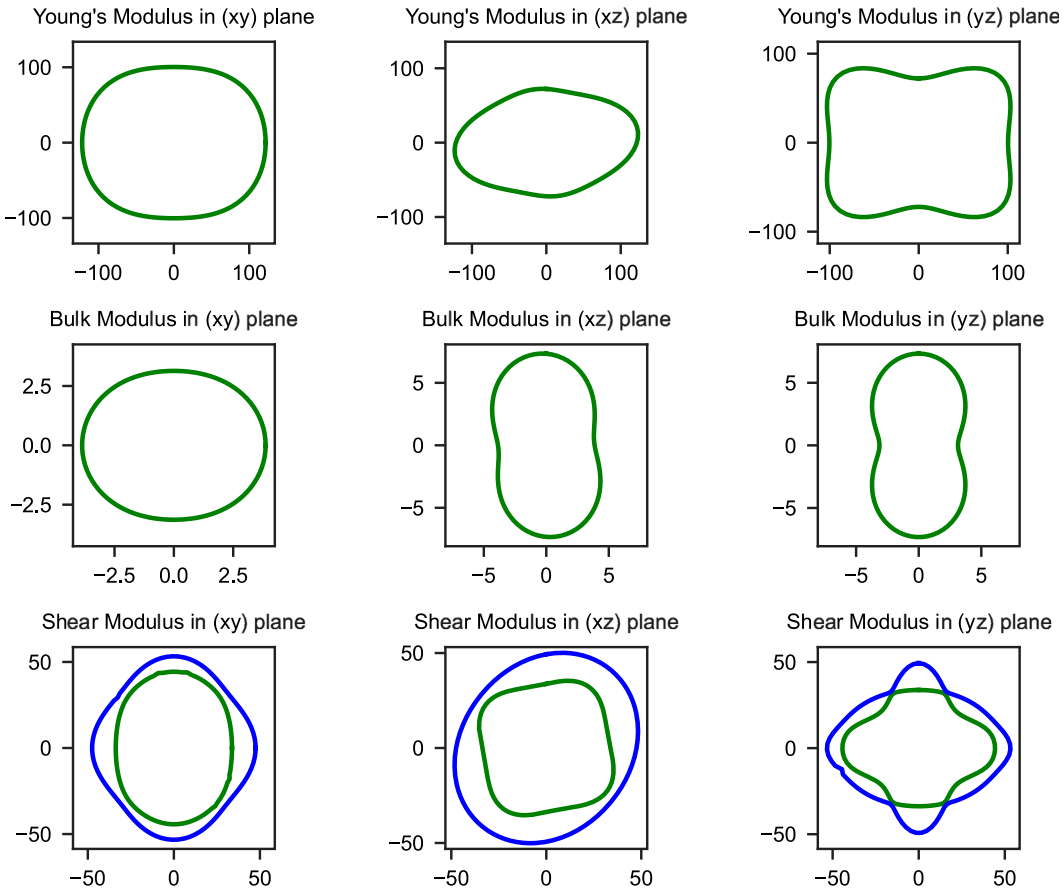

Fig. 3. Calculated spatial dependence of Young's modulus, Bulk modulus, and shear modulus (blue and green indicate the maximum and minimum values, respectively) of SVY. (For interpretation of the references to color in this figure legend, the reader is referred to the web version of this article.)

approach employed in this study. By assessing the agreement between the calculated and experimental values, we can evaluate the predictive ability of the computational method and gain confidence in its ability to accurately capture the elastic behavior of the CAS phases. It is worth noting that obtaining experimental data for the elastic properties of CAS phases can be challenging due to the complexity of the materials and the difficulties associated with their characterization.

Table 7 provides the DFT-calculated mechanical properties together with Pugh's ratio (K/G) and the universal elastic anisotropy index (A^U) for the CAS phases. For the ANO phase, the DFT-PBE-D2 calculations in this work yields an excellent agreement of mechanical properties with experimental data [39]. For SVY, the DFT-PBE-D2 calculations in this work gives a bulk modulus (K) of 71 GPa. Comparing the DFT-calculated bulk modulus values of ANO and SVY, ANO exhibits a higher bulk modulus (83 GPa) compared to SVY (71 GPa). This suggests that ANO is stiffer and more resistant to volume changes under pressure than SVY. Experimental data from Refs. [40,41] cover a range of bulk modulus values of 65–69 GPa for SVY. Unfortunately, no experimental data has been found for other elastic properties for SVY. Another theoretical work [21] using the DFT-LDA method yields a bulk modulus (K) value of 20 GPa for the CAS glass with a similar composition to SVY. The obtained value of 20 GPa is significantly lower than both the DFT-PBE-D2 calculations in this work (83 GPa) and the experimental range (69 GPa, 67–65 GPa). This suggests that the DFT-LDA method, with its simplified exchange–correlation functional, is not suitable for accurately predicting the bulk modulus of CAS materials.

The elastic anisotropy index (A^U) provides a measure of the degree of anisotropy in the elastic properties of a material. Comparing the values of A^U for ANO and SVY, we observe that ANO has a higher A^U value of 0.94, while SVY has a lower A^U value of 0.32. This indicates that ANO exhibits a higher degree of elastic anisotropy compared to SVY. The anisotropy of ANO depicted in Fig. 2 demonstrates a greater degree of variation compared to both the SVY (Fig. 3) and SCO (Fig. 4). Although it may be challenging to discern these differences visually by examining Figures alone, the numerical data provided in Table 7 provides concrete evidence supporting this observation. The higher A^U value for ANO suggests that its elastic properties are more direction-dependent, indicating stronger variations in its mechanical response along different crystallographic orientations. On the other hand, the lower A^U value for SVY suggests a more isotropic behavior, where its elastic properties are less influenced by the crystallographic orientation. The distinct crystallography of ANO and SVY gives rise to differences in their atomic arrangements, bonding patterns, and symmetries. These structural disparities directly impact the mechanical response of the materials, including their elastic properties. Therefore, despite of having the same chemical composition, ANO and SVY exhibit different elastic constants, such as bulk modulus (K), shear modulus (G), and Young's modulus (E).

The bulk modulus (K) values of SCO obtained from this work using DFT-PBE-D2 are 53 GPa for SCO and 38 GPa for SCO-D. This value is in line with the experimental data from previous studies reported by Ballone et al. [40] and Gatta et al. [41]. It is important to note that there can be variations in the experimental conditions and sample quality, which may contribute to discrepancies between the calculated and experimental values. Furthermore, the DFT-PBE results by Bryukhanov et al. [25] show a higher K value compared to both the present study and the experimental data. This discrepancy could arise from the dispersion correction in DFT-PBE approach. Overall, while there are some differences between the calculated and experimental values, the DFT-PBE-D2 results in this work provide reasonable estimates for the bulk modulus of SCO and SCO-D.

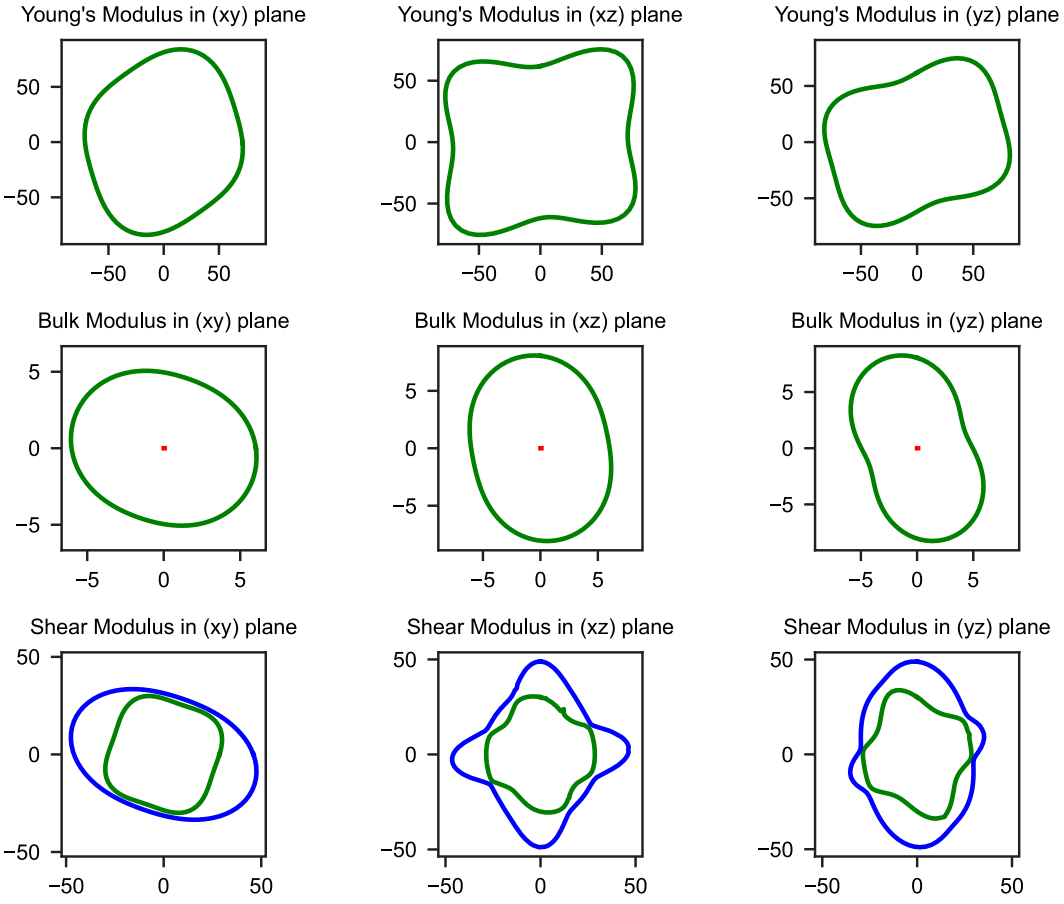

Fig. 4. Calculated spatial dependence of Young's modulus, Bulk modulus, and shear modulus (blue and green indicate the maximum and minimum values, respectively) of SCO. (For interpretation of the references to color in this figure legend, the reader is referred to the web version of this article.)

The dehydration of SCO to form SCO-D exhibits an interesting effect on the elastic properties. Comparing the mechanical moduli, SCO-D has a value comparable to SCO obtained in this work using DFT-PBE-D2. This reduction indicates a decrease in the resistance to volume changes upon dehydration. Moreover, the dehydration of SCO-D leads to an increase in the universal elastic anisotropy index. The A^U value for SCO-D (1.28) is higher than that of SCO (0.39), indicating a greater degree of elastic anisotropy in SCO-D. This suggests that the structural changes induced by dehydration result in a more pronounced directional dependence of the elastic properties of SCO-D (see Fig. 5) compared to SCO. The observed reduction in elastic properties and the increase in the universal elastic anisotropy in SCO-D due to dehydration highlights the significant influence of water molecules on the mechanical behavior of the material. These findings provide insights into the structural and mechanical transformations that occur during the dehydration process and contribute to a better understanding of the role of water molecules in dictating the elastic properties of CAS phases.

The mechanical analysis of the crystalline phases in CAS revealed interesting findings regarding their brittleness. We calculated the Pugh's ratio for CAS phases as a metric to assess their level of ductility versus brittleness. The resulting values ranged from 1.6 to 2.2 (Table 7), with the boundary between these two properties being marked at a value of 1.75. Lower values denote increased brittleness, while higher values represent ductility. Among the CAS phases, only ANO exhibits a Pugh's ratio of 2.2, indicating ductile behavior. The remaining phases have ratios lower than 1.75, which signifies that they are mainly brittle.

Table 7
DFT calculated mechanical properties of bulk modulus K, young's modulus E, shear moduli G , Poisson ratio v, Pugh's ratio K/G, and universal elastic anisotropy index A^U of CAS phases. The available experimental values are included for comparison.

Phase	K (GPa)	G (GPa)	E (GPa)	v	K/G	A^U
ANO						
DFT-PBE-D2 (this work)	83	39	100	0.30	2.2	0.94
Exp.[39]	92	42	/	0.31	/	/
SVY						
DFT-PBE-D2 (this work)	71	41	103	0.26	1.7	0.32
Exp.[22,23]	69, 67–65	/	/	/	/	/
DFT-LDA [21]	20	/	/	/	/	/
SCO						
DFT-PBE-D2(this work)	53	32	80	0.25	1.6	0.39
Exp.[40,41]	61, 56	/	/	/	/	/
DFT-PBE [25]	66	/	/	/	/	/
SCO-D						
DFT-PBE-D2(this work)	38	24	60	0.24	1.6	1.28
Exp.	/	/	/	/	/	/

3.3. Electronic properties

In this section, our objective is to examine the electronic structure of CAS by analyzing the individual contributions of each atom type, namely Ca, Al, Si, O, and H, to the total density of states (DOS). Here, E represents the energy of electronic states within a material, and E_F is the energy of Fermi level. To ensure consistency of the calculations, the energy of the Fermi level (E_F) was set as the reference point. By studying the DOS, we gained insight into the distribution and occupancy of electronic states and their dependence on the different atomic species present in CAS.

Fig. 6 and Fig. 7 shows the results of the analysis for ANO and SVY, respectively. Since these two phases share the same chemical composition, it is expected that their DOS profiles are similar. The presented figure confirms this expectation, illustrating that both oxygen

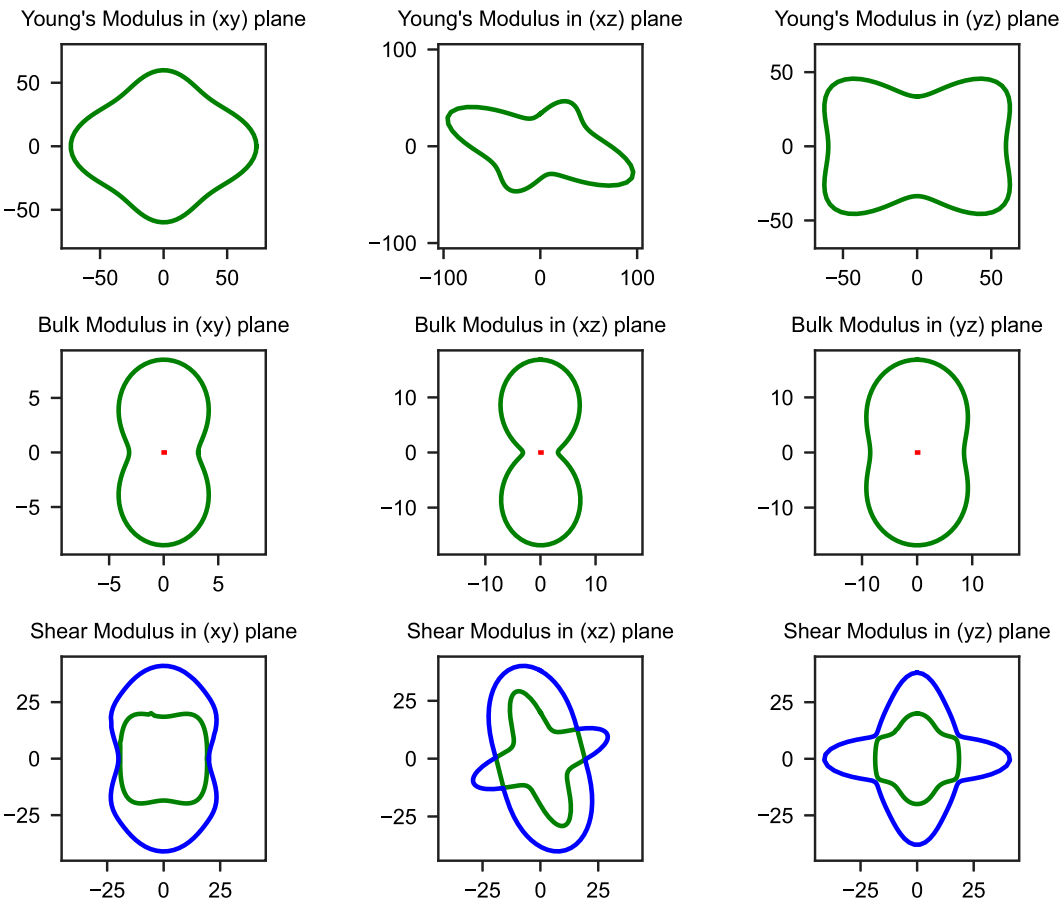

Fig. 5. Calculated spatial dependence of Young's modulus, Bulk modulus, and shear modulus (blue and green indicate the maximum and minimum values, respectively) of SCO-D. (For interpretation of the references to color in this figure legend, the reader is referred to the web version of this article.)

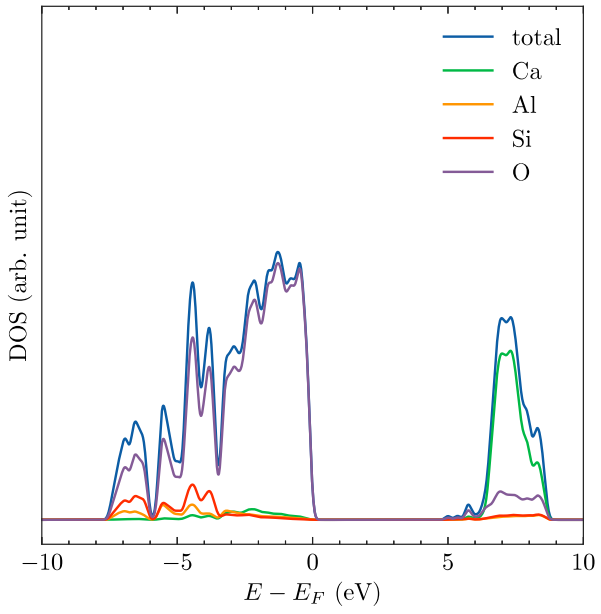

Fig. 6. Total Density of State with atomic contributions of ANO.

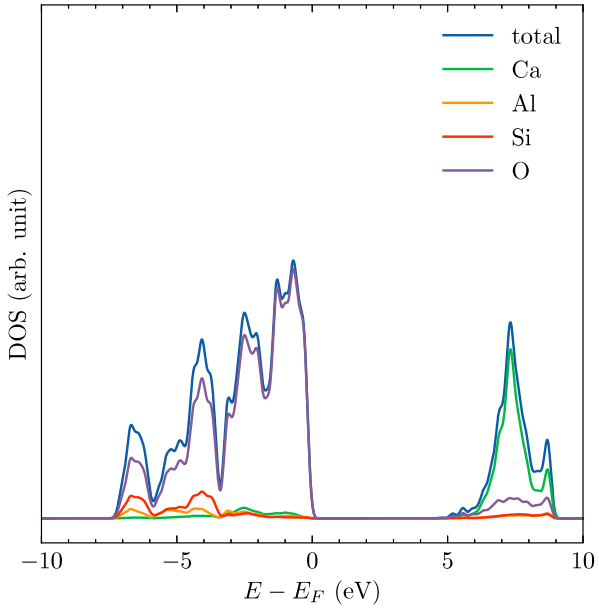

Fig. 7. Total Density of State with atomic contributions of SVY.

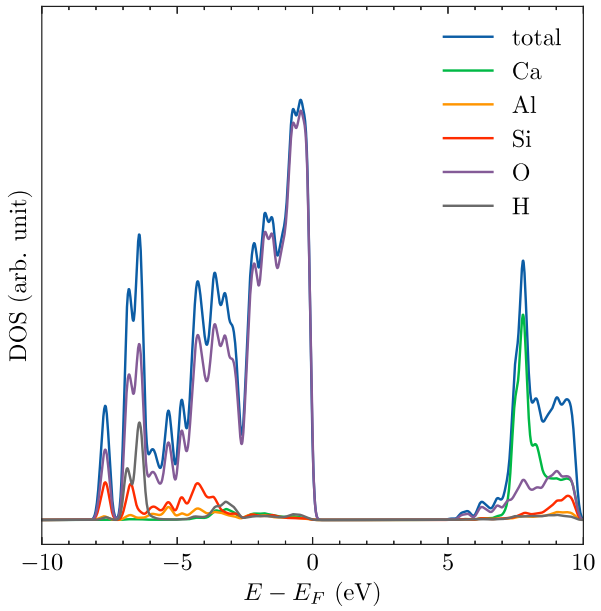

Fig. 8. Total Density of State with atomic contributions of SCO.

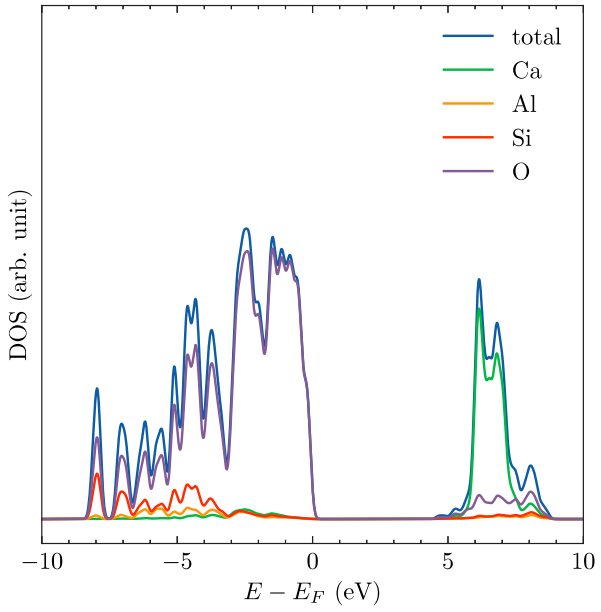

Fig. 9. Total Density of State with atomic contributions of SCO-D.

and calcium atoms contribute significantly to the valence region of the DOS. These contributions suggest that the atomic species are primarily involved in the formation of electronic states within the energy range associated with valence electrons.

Conversely, the analysis reveals that the conductive region of the DOS is primarily dominated by calcium atoms, whereas oxygen atoms contribute less (see Fig. 6). This observation suggests that the electronic states responsible for conducting properties are mainly associated with the calcium atoms within the CAS phases. Furthermore, the investigation confirms that the contributions of silicon (Si) and aluminum (Al) atoms to the total DOS are negligible.

Figs. 8 and 9 present the DOS plots for SCO and SCO-D, respectively. In terms of the DOS contributions, we find remarkable similarities between SCO and the previously examined ANO phase. The similarity is anticipated due to their shared chemical composition within the CAS framework. Specifically, our analysis reveals that both oxygen and calcium atoms give substantial contributions to the valence region of the DOS in SCO, similar to their role in ANO. An interesting observation is the limited contribution of hydrogen atoms to the total DOS in SCO. This finding aligns with the expectations, as hydrogen atoms typically exhibit a minimal impact on the electronic structure of materials due to their low atomic number and relatively low electron density.

Comparing the DOS profiles of SCO and SCO-D, we note a high degree of similarity between these two structures. This outcome is also reasonable, as SCO-D is derived from SCO through the process of dehydration. The preservation of the DOS features, despite the removal of water molecules, suggests that the electronic structure of SCO remains largely unaffected by the dehydration process. Consequently, the DOS patterns of SCO and SCO-D display notable similarities.

The DFT calculated band-gap values of ANO, SVY, SCO and SCO-D are 5.10 eV, 4.83 eV, 5.65 eV and 4.74 eV, respectively. It is important to note that a direct comparison with existing literature values was not feasible at this time. To the best of our knowledge, the band gaps of these specific phases have not been reported in previous studies. However, these values are consistent with calculated values of other calcium silicate structures, such as C_2S and C_3S phases, which typically fall within the range of 3.4–5.81 eV [30,31,42,43].

3.4. Thermodynamics properties

In this section, the calculated thermodynamic properties of the CAS phases by use of the Finite Differences method [27,28] presented in Section 2. Specifically, we focus on the calculation and analysis of the Helmholtz free energy, entropy, and heat capacity at constant volume (C_v).

The calculated thermodynamic profiles for the ANO and SVY phases are depicted in Fig. 10. As expected, the Helmholtz free energy exhibits a decreasing trend with increasing temperature. In contrast, both the entropy and heat capacity at constant volume show an increasing trend with temperature. This behavior is expected, as the thermal energy promotes greater molecular motion and configurational disorder, resulting in an increase in the system's entropy and its ability to store energy as heat. It is worth emphasizing that the observed thermodynamic profiles for ANO and SVY are identical. The reason for this is that these two phases possess exactly the same chemical composition, $CaAl_2Si_2O_8$.

Fig. 11 presents the thermodynamic properties of SCO and SCO-D, offering insights into their respective characteristics. Notably, the absolute value of thermodynamic properties of SCO-D are consistently lower than those of SCO. This is due to the dehydrated nature of SCO-D, which contains three fewer water molecules per unit cell compared to SCO. The decrease in the absolute value of the thermodynamic properties of SCO-D can be attributed to the removal of water molecules, which results in a reduction in the overall energy and configurational possibilities of the system. Specifically, the removal of water molecules leads to a decrease in the system's Helmholtz free energy, reflecting a lower energy requirement for maintaining its stability. Additionally, the entropy and heat capacity at constant volume (C_v) of SCO-D are lower compared to SCO. This decrease in entropy and C_v can be attributed to the reduced molecular motion and configurational disorder resulting from the absence of water molecules in SCO-D.

To assess the reliability of the thermodynamic calculations, we conducted a comparison between the calculated values and the corresponding experimental data for the entropy and heat capacity of CAS at a reference temperature of $T = 298$ K. Using the DFT-PBE-D2 method, we obtained entropy and heat capacity values of 208 J/mol/K and 212 J/mol/K, respectively, for the ANO phase. The calculated values exhibit excellent agreement with the experimental measurements (202 J/mol/K and 211 J/mol/K), as summarized in Table 8. The deviation between the calculated values and the experimental data for the entropy and heat capacity of SCO is also found to be less than 5%, further validating the accuracy and robustness of the DFT approach

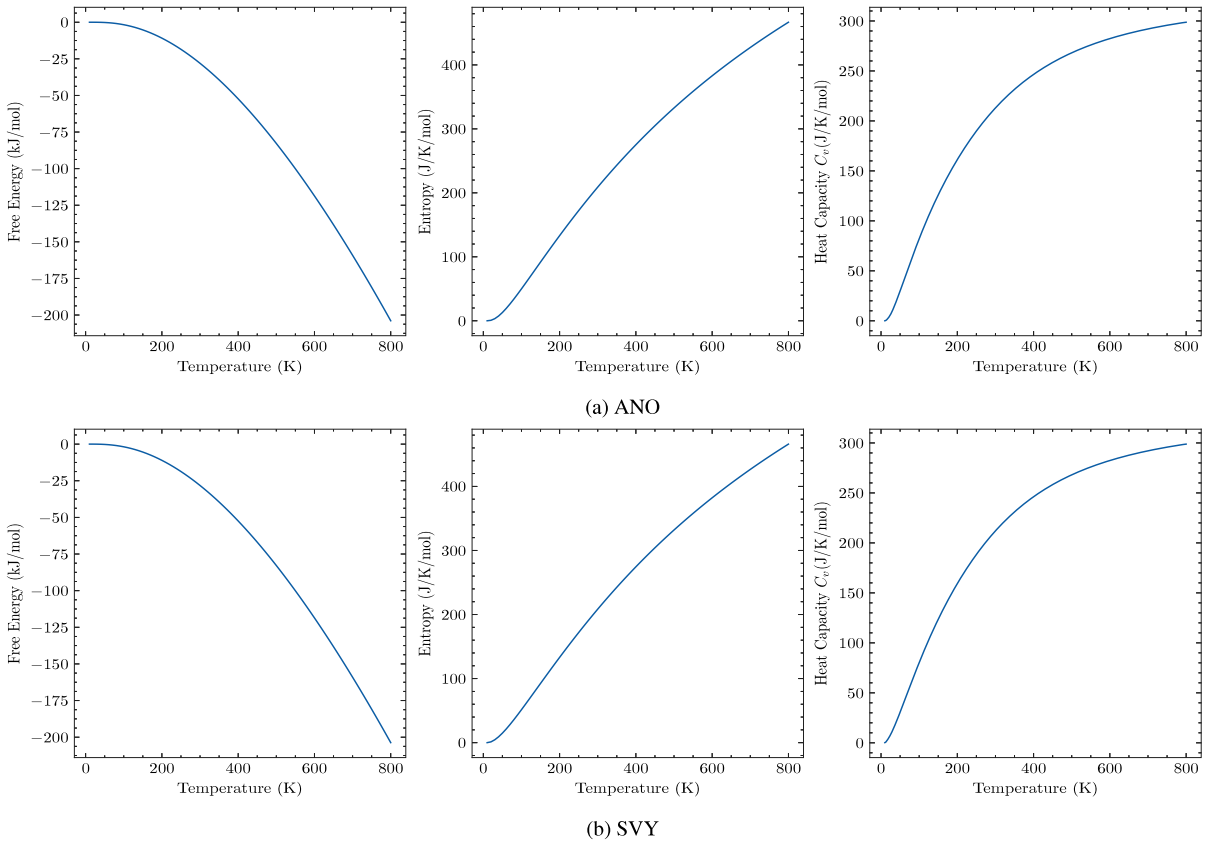

Fig. 10. Calculated thermodynamic properties (Helmholtz free energy, entropy and heat capacity) of ANO and SVY phases for the temperature range of 0 K–800 K.

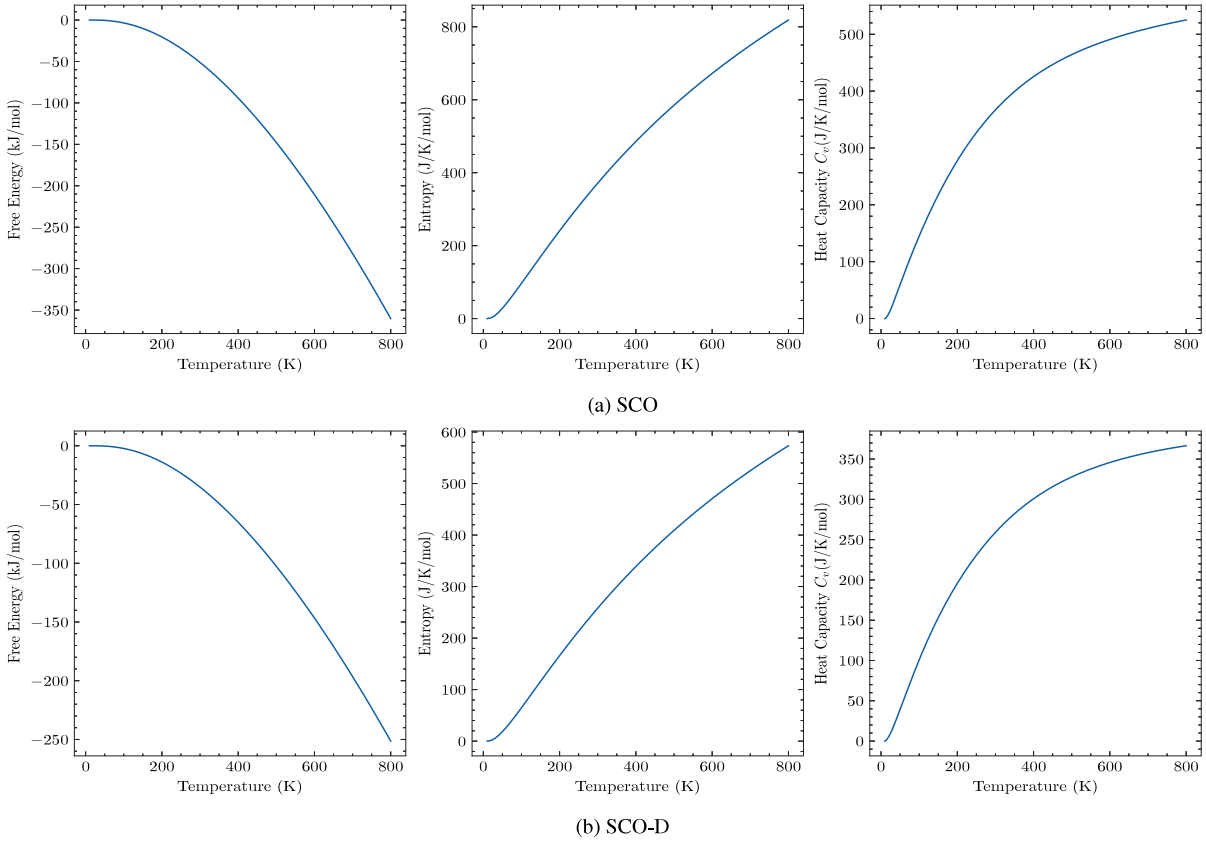

Fig. 11. Calculated thermodynamic properties (Helmholtz free energy, entropy and heat capacity) of SCO and SCO-D phases for the temperature range of 0 K–800 K.

Table 8
Thermochemical properties for CAS phases at the reference temperature 298 K.

Phase	Entropy (J/K/mol)	Heat capacity (J/K/mol)
ANO		
DFT (this work)	208	212
Exp.[44]	202	211
SVY		
DFT (this work)	208	211
SCO		
DFT (this work)	371	368
Exp.[14]	367	382
SCO-D		
DFT (this work)	258	259
Exp.	/	/

for thermodynamic calculations. The close agreement between the calculated and experimental values demonstrates the suitability of the chosen computational methodology and the underlying DFT-PBE-D2 approximation for accurately capturing the thermodynamic behavior of CAS phases.

While the absence of experimental data for SVY and SCO-D limits our ability to perform a direct comparison, the reasonable trends and consistent behavior observed in the calculated results supports the reliability and accuracy of the computational approach. These findings provide valuable insights into the thermodynamic properties of SVY and SCO-D, contributing to a better understanding of their stability, behavior, and potential applications. According to the calculations, the entropy and heat capacity of the dehydrated SCO-D phase are found to be approximately 30% lower than those of the hydrated SCO phase. The significant reduction can be attributed to the removal of water molecules from the crystal structure of SCO-D, leading to a decrease in the degrees of freedom and vibrational modes available to the system. As a result, the overall thermal contributions, reflected in the entropy and heat capacity values, are substantially diminished in the dehydrated phase.

To improve the understanding of the thermodynamic properties of SVY and SCO-D, future experimental investigations are warranted. The availability of experimental data would not only enable a more robust validation of our computational results but also facilitate a deeper exploration of the structural transformations, phase transitions, and thermodynamic characteristics associated with these dehydrated phases.

3.5. The effect of polymorphism and dehydration

Polymorphism, the ability of a material to exist in different crystal structures while maintaining the same chemical composition, and dehydration, the removal of water molecules from a hydrated compound, can have a significant influence on the properties and behavior of CAS phases. In the following, we will discuss the impact of polymorphs and dehydration on the structural, mechanical, electronic, and thermodynamic properties of CAS phases.

In the case of ANO (anorthite) and SVY (svyatoslavite), despite of having the same chemical composition of $CaAl_2Si_2O_8$, they exhibit distinct crystal structures. The polymorphic transformation from ANO to SVY involves changes in lattice parameters, coordination environments, and packing motifs. The mechanical strength, including properties like hardness, strength, and elasticity, can vary significantly between ANO and SVY due to their different crystal structures. The arrangement of atoms and the bonding interactions within the crystal lattice influence the resistance to deformation and the ability to withstand mechanical stresses. Consequently, ANO and SVY may exhibit contrasting mechanical responses under applied loads.

Despite of the differences in mechanical strength, the electronic and thermodynamic properties of ANO and SVY remain the same. The electronic structure, including the density of states, band gaps, and electronic band structures, is governed by the chemical composition rather than the specific crystal structure. Likewise, the thermodynamic properties, such as the Helmholtz free energy, entropy, and heat capacity, are primarily influenced by the chemical composition and the atomic interactions within the crystal lattice. While polymorphism can lead to variations in the mechanical properties of ANO and SVY, their identical chemical compositions result in similar thermodynamic characteristics.

When CAS phases undergo dehydration, the removal of water molecules from their structures leads to notable changes in their physical and chemical properties. Taking the example of SCO and SCO-D, the removal of water molecules results in a reduction in the unit volume of the crystal structure. The presence of water molecules in SCO contributes to the intermolecular interactions, occupying specific positions within the lattice. The removal of these water molecules disrupts these interactions, leading to a decrease in the unit volume of SCO-D compared to SCO.

The dehydration process also has a significant impact on the mechanical strength of the CAS phases. The mechanical properties, including stiffness, hardness, and resistance to deformation, are closely related to the interatomic bonding and structural integrity of the material. The removal of water molecules from SCO-D weakens the intermolecular interactions and alters the atomic arrangement within the crystal lattice, resulting in a reduction of mechanical strength compared to the hydrated form of SCO. Furthermore, the absolute values of thermodynamic properties of SCO-D are significantly lower than those of SCO due to the absence of water molecules. Thermodynamic parameters such as Helmholtz free energy, entropy, and heat capacity are influenced by the molecular vibrations, rotational motions, and configurational changes within the crystal lattice. The presence of water molecules in SCO contributes to the vibrational and rotational degrees of freedom.

4. Concluding remarks

This study employs first principles atomistic simulations based on the DFT-PBE-D2 method to investigate the mechanical, electronic, and thermodynamical properties of the following crystalline phases of calcium aluminosilicate (CAS): anorthite (ANO), svyatoslavite (SVY), scolecite (SCO), and Dehydrated scolecite (SCO-D). Investigating the structural features and mechanical behavior of stone wool materials derived from CAS phases could provide valuable insights for optimizing their thermal and acoustic insulation properties. The obtained results have led to several significant conclusions:

- Polymorphism plays a significant role in determining the mechanical strength of CAS phases. The distinct crystal structures of ANO and SVY result in different mechanical properties, while their electronic and thermodynamic behaviors remain similar.
- Dehydration has a pronounced effect on CAS phases, causing a reduction in unit volume and mechanical strength. The absence of water molecules weakens intermolecular interactions, leading to decreased mechanical properties in dehydrated phases such as SCO-D.
- Thermodynamic properties, including entropy, heat capacity, and Helmholtz free energy, are strongly influenced by the presence or absence of water molecules in CAS phases. Dehydrated phases exhibit significantly lower absolute values for the thermodynamic properties due to the absence of water, which contributes to vibrational and rotational degrees of freedom.
- The calculated elastic and thermodynamic properties are in excellent agreement with the available experimental data. This demonstrates the advantage and accuracy of the computational approach of DFT-PBE-D2 of this study. Further experimental investigations of the mechanical properties as well as the thermodynamic properties of SCO-D and SVY, would contribute to a more complete understanding of these CAS phases.

- These crystalline phases exhibit a complex interplay between their crystal structures and mechanical properties, which are highly relevant to stone wool materials used in insulation. Additionally, understanding the effects of polymorphism and dehydration on the performance of stone wool materials can guide the development of enhanced insulation materials with improved mechanical strength, durability, and thermal efficiency.
- Future research efforts in this field could expand beyond the investigation of crystalline phases to encompass the study of non-crystalline or amorphous components present in stone wool materials. Additionally, exploring adsorption processes involving water molecules on both crystalline and non-crystalline phases can provide valuable insights into the behavior of stone wool under various environmental conditions. This knowledge may lead to improvements in moisture management strategies and ultimately enhance the durability and efficiency of insulation products used across diverse industries.

CRediT authorship contribution statement

Thi H. Ho: Writing – original draft, Investigation, Formal analysis, Data curation. **Do Tuong Ha:** Writing – review & editing, Formal analysis. **Nguyen-Hieu Hoang:** Writing – review & editing, Funding acquisition, Formal analysis. **Øivind Wilhelmsen:** Writing – review & editing, Resources, Conceptualization. **Thuat T. Trinh:** Writing – review & editing, Supervision, Project administration, Methodology, Conceptualization.

Declaration of competing interest

The authors declare that they have no known competing financial interests or personal relationships that could have appeared to influence the work reported in this paper.

Data availability

Data will be made available on request.

Acknowledgments

The computational resource was partially provided by Van Lang University and Norwegian University of Science and Technology. N–HH acknowledges the COMPASS project (funding from the European Union Horizon Europe program under the grant agreement 101084623) and the HotCaSe project (Research Council of Norway - grant number NFR269399). ØW and TTT acknowledge funding from the Research Council of Norway (RCN), the Center of Excellence Funding Scheme, Project No. 262644, PoreLab. Funding for ØW was also provided by the PredictCUI project coordinated by SINTEF Energy Research, and the authors acknowledge the contributions of Equinor, Gassco, Shell, and the PETROMAKS 2 programme of the Research Council of Norway (308770).

References

[1] A.C. Schmidt, A.A. Jensen, A.U. Clausen, O. Kamstrup, D. Postlethwaite, A comparative Life Cycle assessment of building insulation products made of stone wool, paper wool and flax, Int. J. LCA 9 (1) (2004) 53–66, http://dx.doi.org/10.1007/bf02978536.

[2] A. Karamanos, S. Hadiarakou, A. Papadopoulos, The impact of temperature and moisture on the thermal performance of stone wool, Energy Build. 40 (8) (2008) 1402–1411, http://dx.doi.org/10.1016/j.enbuild.2008.01.004.

[3] A.A. Stec, T.R. Hull, Assessment of the fire toxicity of building insulation materials, Energy Build. 43 (2–3) (2011) 498–506, http://dx.doi.org/10.1016/j.enbuild.2010.10.015.

[4] M.M. Smedskjaer, M. Solvang, Y. Yue, Crystallisation behaviour and high-temperature stability of stone wool fibres, J. Eur. Ceram. Soc. 30 (6) (2010) 1287–1295, http://dx.doi.org/10.1016/j.jeurceramsoc.2009.12.009.

[5] M.D. Lund, Y.-Z. Yue, Influences of chemical aging on the surface morphology and crystallization behavior of basaltic glass fibers, J. Non-Cryst. Solids 354 (12–13) (2008) 1151–1154, http://dx.doi.org/10.1016/j.jnoncrysol.2006.11.031.

[6] A. Ivanič, G. Kravanja, W. Kidess, R. Rudolf, S. Lubej, The influences of moisture on the mechanical, morphological and thermogravimetric properties of mineral wool made from basalt glass fibers, Materials 13 (10) (2020) 2392, http://dx.doi.org/10.3390/ma13102392.

[7] M. Turchi, S. Perera, S. Ramsheh, A. Popel, D. Okhrimenko, S. Stipp, M. Solvang, M. Andersson, T. Walsh, Predicted structures of calcium aluminosilicate glass as a model for stone wool fiber: Effects of composition and interatomic potential, J. Non-Cryst. Solids 567 (2021) 120924, http://dx.doi.org/10.1016/j.jnoncrysol.2021.120924.

[8] D. Cao, Fusion joining of thermoplastic composites with a carbon fabric heating element modified by multiwalled carbon nanotube sheets, Int. J. Adv. Manuf. Technol. 128 (9–10) (2023) 4443–4453, http://dx.doi.org/10.1007/s00170-023-12202-6.

[9] D. Cao, D. Bouzolin, H. Lu, D.T. Griffith, Bending and shear improvements in 3D-printed core sandwich composites through modification of resin uptake in the skin/core interphase region, Composites B 264 (None) (2023) 110912, http://dx.doi.org/10.1016/j.compositesb.2023.110912.

[10] D. Cao, Enhanced buckling strength of the thin-walled continuous carbon fiber–reinforced thermoplastic composite through dual coaxial nozzles material extrusion process, Int. J. Adv. Manuf. Technol. 128 (3–4) (2023) 1305–1315, http://dx.doi.org/10.1007/s00170-023-12014-8.

[11] K. Traoré, T.S. Kabré, P. Blanchart, Gehlenite and anorthite crystallisation from kaolinite and calcite mix, Ceram. Int. 29 (4) (2003) 377–383, http://dx.doi.org/10.1016/s0272-8842(02)00148-7.

[12] H.D. Megaw, C. Kempster, E. Radoslovich, The structure of anorthite, CaAl2Si2O8. II. description and discussion, Acta Crystallogr. 15 (10) (1962) 1017–1035.

[13] S. Krivovichev, E. Shcherbakova, T. Nishanbaev, The crystal structure of svyatoslavite and evolution of complexity during crystallization of a CaAl2Si2O8 melt: A structural automata description, Canadian Mineral. 50 (3) (2012) 585–592, http://dx.doi.org/10.3749/canmin.50.3.585.

[14] G. Johnson, H. Flotow, P. O'Hare, W. Wise, Thermodynamic studies of zeolites; natrolite, mesolite and scolecite, Am. Mineral. 68 (11–12) (1983) 1134–1145.

[15] J. Zhang, J. Yang, D. Hou, Q. Ding, Molecular dynamics study on calcium aluminosilicate hydrate at elevated temperatures: Structure, dynamics and mechanical properties, Mater. Chem. Phys. 233 (2019) 276–287, http://dx.doi.org/10.1016/j.matchemphys.2019.05.020.

[16] G. Agnello, R. Youngman, L. Lamberson, N. Smith, W. LaCourse, A.N. Cormack, Bulk structures of silica-rich calcium aluminosilicate (CAS) glasses along the molar CaO/Al2O3=1 join via molecular dynamics (MD) simulation, J. Non-Cryst. Solids 519 (2019) 119450, http://dx.doi.org/10.1016/j.jnoncrysol.2019.05.026.

[17] P. Ganster, M. Benoit, J.-M. Delaye, W. Kob, Surface of a calcium aluminosilicate glass by classical and ab initio molecular dynamics simulations, Surf. Sci. 602 (1) (2008) 114–125, http://dx.doi.org/10.1016/j.susc.2007.09.047.

[18] J. Zhou, Y. Liang, Reactive molecular dynamics simulation on the structure characteristics and tensile properties of calcium silicate hydrate at various temperatures and strain rates, Mol. Simul. 46 (15) (2020) 1181–1190, http://dx.doi.org/10.1080/08927022.2020.1807543.

[19] K.V. Tian, M.Z. Mahmoud, P. Cozza, S. Licoccia, D.-C. Fang, D. Di Tommaso, G.A. Chass, G.N. Greaves, Periodic vs. molecular cluster approaches to resolving glass structure and properties: Anorthite a case study, J. Non-Cryst. Solids 451 (2016) 138–145, http://dx.doi.org/10.1016/j.jnoncrysol.2016.06.027.

[20] F. Zhang, X. Liu, X. He, J. Zhao, W. Chu, Y. Xue, A periodic density functional theory study of adsorption of CO₂ on anorthite (001) surface and effect of water, J. Theor. Comput. Chem. 18 (02) (2019) 1950010, http://dx.doi.org/10.1142/s021963361950010x.

[21] D.B. Ghosh, B.B. Karki, First-principles molecular dynamics simulations of anorthite (CaAl2Si2O8) glass at high pressure, Phys. Chem. Mineral. 45 (6) (2018) 575–587, http://dx.doi.org/10.1007/s00269-018-0943-4.

[22] A. Pönitzsch, M. Nofz, L. Wondraczek, J. Deubener, Bulk elastic properties, hardness and fatigue of calcium aluminosilicate glasses in the intermediate-silica range, J. Non-Cryst. Solids 434 (2016) 1–12, http://dx.doi.org/10.1016/j.jnoncrysol.2015.12.002.

[23] V. Askarpour, M.H. Manghnani, P. Richet, Elastic properties of diopside, anorthite, and grossular glasses and liquids: A Brillouin scattering study up to 1400 K, J. Geophys. Res. 98 (B10) (1993) 17683–17689, http://dx.doi.org/10.1029/93jb01558.

[24] M. Fischer, Structure and bonding of water molecules in zeolite hosts: Benchmarking plane-wave DFT against crystal structure data, Z. Kristallogr. 230 (5) (2015) 325–336, http://dx.doi.org/10.1515/zkri-2014-1809.

[25] I.A. Bryukhanov, A.A. Rybakov, A.V. Larin, D.N. Trubnikov, D.P. Vercauteren, The role of water in the elastic properties of aluminosilicate zeolites: Dft investigation, J. Mol. Model. 23 (3) (2017) 1–12, http://dx.doi.org/10.1007/s00894-017-3237-8.

[26] American Mineralogist Crystal Structure Database — rruff.geo.arizona.edu, http://rruff.geo.arizona.edu/AMS/amcsd.php, [Accessed 16-11-2023].

[27] G. Kresse, J. Hafner, Ab initio molecular dynamics for liquid metals, Phys. Rev. B 47 (1) (1993) 558.
[28] G. Kresse, J. Furthmüller, Efficiency of ab-initio total energy calculations for metals and semiconductors using a plane-wave basis set, Comput. Mater. Sci. 6 (1) (1996) 15–50, http://dx.doi.org/10.1016/0927-0256(96)00008-0.
[29] H. Manzano, E. Durgun, M.J. Abdolhosseine Qomi, F.-J. Ulm, R. Pellenq, J. Grossman, Impact of chemical impurities on the crystalline cement clinker phases determined by atomistic simulations, Cryst. Growth Des. 11 (7) (2011) 2964–2972, http://dx.doi.org/10.1021/cg200212c.
[30] M. Laanaiya, A. Bouibes, A. Zaoui, Understanding why Alite is responsible of the main mechanical characteristics in Portland cement, Cem. Concr. Res. 126 (2019) 105916, http://dx.doi.org/10.1016/j.cemconres.2019.105916.
[31] N.L. Mai, N.-H. Hoang, H.T. Do, M. Pilz, T.T. Trinh, Elastic and thermodynamic properties of the major clinker phases of Portland cement: Insights from first principles calculations, Constr. Build. Mater. 287 (2021) 122873, http://dx.doi.org/10.1016/j.conbuildmat.2021.122873.
[32] S. Grimme, J. Antony, S. Ehrlich, H. Krieg, A consistent and accurate ab initio parametrization of density functional dispersion correction (DFT-d) for the 94 elements H-Pu, J. Chem. Phys. 132 (15) (2010) 154104, http://dx.doi.org/10.1063/1.3382344.
[33] K. Momma, F. Izumi, VESTA 3for three-dimensional visualization of crystal, volumetric and morphology data, J. Appl. Cryst. 44 (6) (2011) 1272–1276, http://dx.doi.org/10.1107/s0021889811038970.
[34] R. Gaillac, P. Pullumbi, F.-X. Coudert, ELATE: An open-source online application for analysis and visualization of elastic tensors, J. Phys.: Condens. Matter 28 (27) (2016) 275201, http://dx.doi.org/10.1088/0953-8984/28/27/275201.
[35] N.O. Ongwen, E. Ogam, H.O. Otunga, Ab initio study of elastic properties of orthorhombic cadmium stannate as a substrate for the manufacture of MEMS devices, Mater. Today Commun. 26 (2021) 101822, http://dx.doi.org/10.1016/j.mtcomm.2020.101822.
[36] S.I. Ranganathan, M. Ostoja-Starzewski, Universal elastic anisotropy index, Phys. Rev. Lett. 101 (5) (2008) 055504, http://dx.doi.org/10.1103/physrevlett.101.055504.
[37] N.O. Ongwen, E. Ogam, Z. Fellah, H.O. Otunga, A.O. Oduor, M. Mageto, Accurate ab-initio calculation of elastic constants of anisotropic binary alloys: A case of Fe–Al, Solid State Commun. 353 (2022) 114879, http://dx.doi.org/10.1016/j.ssc.2022.114879.
[38] A. Zaoui, Insight into elastic behavior of calcium silicate hydrated oxide (C–S–H) under pressure and composition effect, Cem. Concr. Res. 42 (2) (2012) 306–312, http://dx.doi.org/10.1016/j.cemconres.2011.10.003.
[39] R.C. Liebermann, A. Ringwood, Elastic properties of anorthite and the nature of the lunar crust, Earth Planet. Sci. Lett. 31 (1) (1976) 69–74, http://dx.doi.org/10.1016/0012-821x(76)90097-2.
[40] P. Ballone, S. Quartieri, A. Sani, G. Vezzalini, High-pressure deformation mechanism in scolecite: A combined computational-experimental study, Am. Mineral. 87 (8–9) (2002) 1194–1206, http://dx.doi.org/10.2138/am-2002-8-919.
[41] G.D. Gatta, A comparative study of fibrous zeolites under pressure, ejm 17 (3) (2005) 411–422, http://dx.doi.org/10.1127/0935-1221/2005/0017-0411.
[42] E. Durgun, H. Manzano, R. Pellenq, J.C. Grossman, Understanding and controlling the reactivity of the calcium silicate phases from first principles, Chem. Mater. 24 (7) (2012) 1262–1267, http://dx.doi.org/10.1021/cm203127m.
[43] H.-J. Hou, W.-X. Chen, H.-J. Zhu, X.-W. Lu, S.-R. Zhang, Q.-F. Zhang, Analysis of the structural, elastic constants, electronic, optical, dynamical, and thermodynamic in dicalcium silicate with various pressures, Vacuum 210 (2023) 111869, http://dx.doi.org/10.1016/j.vacuum.2023.111869.
[44] E. King, Low temperature heat capacities and entropies at 298.15°K. of some crystalline silicates containing calcium, J. Am. Chem. Soc. 79 (20) (1957) 5437–5438, http://dx.doi.org/10.1021/ja01577a028.